LETTERS
PUBLISHED ONLINE: 17 AUGUST 2015 | DOI: 10.1038/NMAT4387
nature materials

Orientational order of motile defects in active nematics

Stephen J. DeCamp†, Gabriel S. Redner†, Aparna Baskaran, Michael F. Hagan* and Zvonimir Dogic*

The study of liquid crystals at equilibrium has led to fundamental insights into the nature of ordered materials, as well as to practical applications such as display technologies. Active nematics are a fundamentally different class of liquid crystals, driven away from equilibrium by the autonomous motion of their constituent rod-like particles[1–4]. This internally generated activity powers the continuous creation and annihilation of topological defects, which leads to complex streaming flows whose chaotic dynamics seem to destroy long-range order[5–11]. Here, we study these dynamics in experimental and computational realizations of active nematics. By tracking thousands of defects over centimetre-scale distances in microtubule-based active nematics, we identify a non-equilibrium phase characterized by a system-spanning orientational order of defects. This emergent order persists over hours despite defect lifetimes of only seconds. Similar dynamical structures are observed in coarse-grained simulations, suggesting that defect-ordered phases are a generic feature of active nematics.

Topological defects play important roles in diverse phenomena ranging from high-energy physics and cosmology to traditional condensed-matter systems[12]. For instance, the spontaneous unbinding of dislocation pairs mediates the melting of 2D crystals[13]. Despite their usual role as centres of disorder, defects can also organize into higher-order equilibrium structures with emergent properties, such as liquid-crystalline twist-grain-boundary phases and flux-line lattices in superconductors[14,15]. Far less is understood about the role of defects in active-matter systems, which are driven away from equilibrium by the motion of their constituent particles[16–24]. Previous work on active nematics has demonstrated an instability at large wavelengths[5] which leads to spontaneous defect nucleation and unbinding[6–10]. In contrast to the well-studied passive defects found in equilibrium matter, defects in active nematics are motile[25], and are continuously generated and annihilated, producing a dynamical defect-riddled phase that is inherently out of equilibrium. The observed dynamics are complex and chaotic, and seem to destroy the long-range ordering of the underlying nematic. Here, by tracking thousands of defects over long times, we demonstrate that defects self-organize into a higher-order phase with broken rotational symmetry. The orientational ordering of defects spans macroscopic samples and persists for the sample lifetime of many hours, despite the lifetimes of the constituent defects being orders of magnitude shorter.

Our experimental system is comprised of micrometre-long stabilized microtubules (MTs), streptavidin clusters of biotin-labelled kinesin motors[26] and the non-adsorbing polymer polyethylene glycol (PEG) (Fig. 1a). In a bulk suspension, PEG induces the formation of MT bundles by the depletion mechanism[27,28]. The same interaction also depletes MTs onto a surfactant-stabilized oil/water interface. Centrifugation makes it possible to spin down all the MT bundles onto the interface, leading to the formation of a dense quasi-2D MT film that exhibits local orientational order. Each kinesin cluster binds to multiple MTs. As each motor within the cluster hydrolyses adenosine triphosphate (ATP), it moves towards the plus end of a MT and induces interfilament sliding[29]. This generates extensile mechanical stresses that drive the nematic film away from equilibrium (Fig. 1b). A biochemical regeneration system maintains a constant ATP concentration and powers the system for over 24 h (see Supplementary Methods). We image these active nematics with both fluorescence microscopy and LC-PolScope[30]. LC-PolScope measures the orientation of the nematic director field $\theta(\mathbf{r})$ with pixel resolution. It also measures the magnitude of the birefringence, which reveals the effective thickness of the nematic film, or retardance field $\Delta(\mathbf{r})$ (see Supplementary Fig. 4 for an extended discussion). Using a $\times 4$ objective, we observe the dynamics of the MT film over the entire field of view, corresponding to an area of 2.3×1.7 mm.

In parallel, we have developed a tractable coarse-grained computational model. Our approach employs Brownian dynamics simulations of rigid spherocylinders which, in equilibrium, form a nematic phase[31]. Long-ranged hydrodynamic interactions are omitted, producing an essentially dry system. The length of each constituent rod increases at a constant rate, producing an extensile stress similar to the motor-driven extension of MT bundles (Fig. 1d). On reaching a preset maximum length, a spherocylinder is split in half and two other rods are simultaneously merged, thus keeping the total particle number fixed (see Supplementary Methods). Although inspired by the dynamics of MT bundles, this approach is not meant to quantitatively reproduce specific features of the experimental system, but simply to capture its microscopic symmetries (nematic interparticle alignment and extensile nematic activity).

In equilibrium, nematic defects anneal to minimize the free energy, eventually producing a uniformly aligned state. It is not possible to prepare an analogous state in extensile active nematics, as uniform alignment is inherently unstable to bend deformations[5]. These distortions grow in amplitude and produce a fracture line, terminated at one end by a defect of charge $+1/2$, and by a $-1/2$ defect at the other (Fig. 1c). The asymmetry of $+1/2$ defects causes motor-generated stresses to produce a net propulsive force, leading to extension of the fracture line. Above a critical length, the fracture line self-heals, leaving behind a pair of isolated, oppositely charged defects[9]. For experimental ATP concentration, $+1/2$ defects move at speeds of $\sim 8\,\mu\mathrm{m\,s^{-1}}$. Defects are transient objects; on average, a $+1/2$ defect exists for 40 s before colliding with a $-1/2$ defect and annihilating, leaving behind a uniformly aligned nematic region[32] (Fig. 1c). The system reaches a steady state in which the rate of defect

Department of Physics, Brandeis University, Waltham, Massachusetts 02454, USA. †These authors contributed equally to this work.
*e-mail: hagan@brandeis.edu; zdogic@brandeis.edu

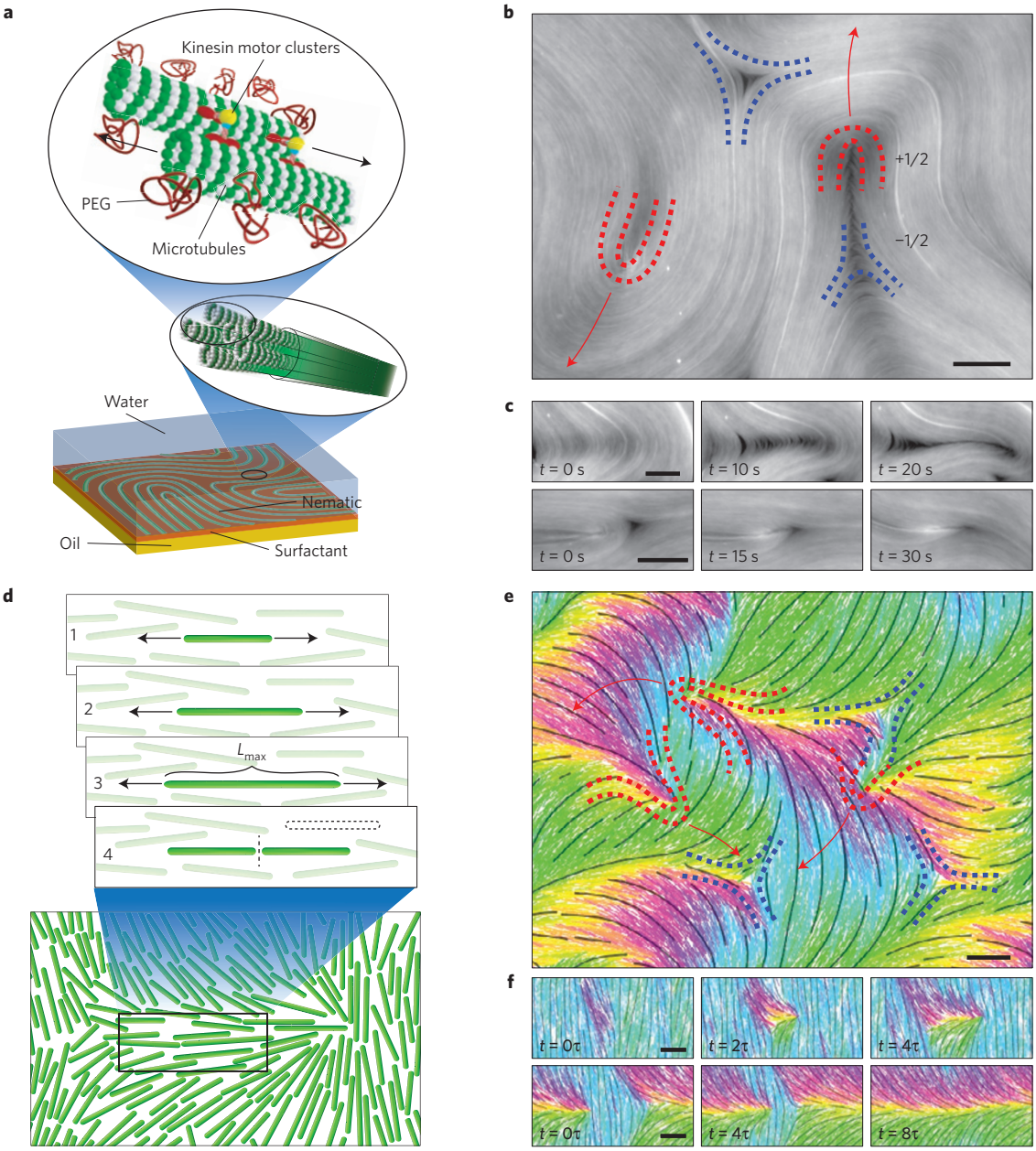

Figure 1 | Overview of the experimental and simulation systems. a, Microtubules (MTs) are bundled together by the depletion agent PEG. Kinesin clusters crosslink MTs and induce interfilament sliding. Bundles are confined to a surfactant-stabilized oil/water interface, where they form a quasi-2D active nematic film. **b**, Fluorescence microscope image of a MT active nematic with defects of charge +1/2 (red) and −1/2 (blue). **c**, Image sequence illustrating the creation (top) and annihilation (bottom) of a defect pair. Scale bars, 50 μm. **d**, Simulation microdynamics, consisting of hard rods that grow and split, reminiscent of the extension of MT bundles. L_{max} is the length at which a rod is split. **e**, Snapshot of a simulated active nematic with marked defects. The colour of a rod indicates its orientation, and black streamlines guide the eye over the coarse-grained nematic field. **f**, Creation (top) and annihilation (bottom) events occur analogously to those in experiments. Scale bars, $2L_{max}$. τ is a dimensionless time unit (Supplementary Information; Section 5).

generation is balanced by the rate of annihilation (Supplementary Movies 1 and 2). Very similar patterns of defect generation and annihilation are observed in the simulations, despite the fact that our computational model does not include hydrodynamic interactions (Fig. 1e,f and Supplementary Movies 4 and 5).

We have developed algorithms that identify defect positions and orientations from either LC-PolScope images or simulation configurations, and that track their temporal dynamics over the entire lifetime of either a MT sample or simulation (see Supplementary Information). Defect positions and orientations are determined by measuring the winding of the local director. We define the orientation of each comet-like +1/2 defect by drawing an arrow from the comet's head to its tail (see Supplementary Information). These algorithms allow us to analyse statistically large defect populations, providing invaluable insight into their self-organization at macroscopic scales.

It has been commonly assumed that the dynamics of motile defects leads to a disordered chaotic state. However, quantitative analyses reveal that this is not the case. In MT samples, we find that the orientational distribution function of +1/2 defects is not flat, but exhibits two well-defined peaks, implying the existence of a higher-order dynamical phase (Fig. 2e). Although +1/2 defects are polar objects, we find that they form a nematic phase in which they are equally likely to point in either direction along the preferred

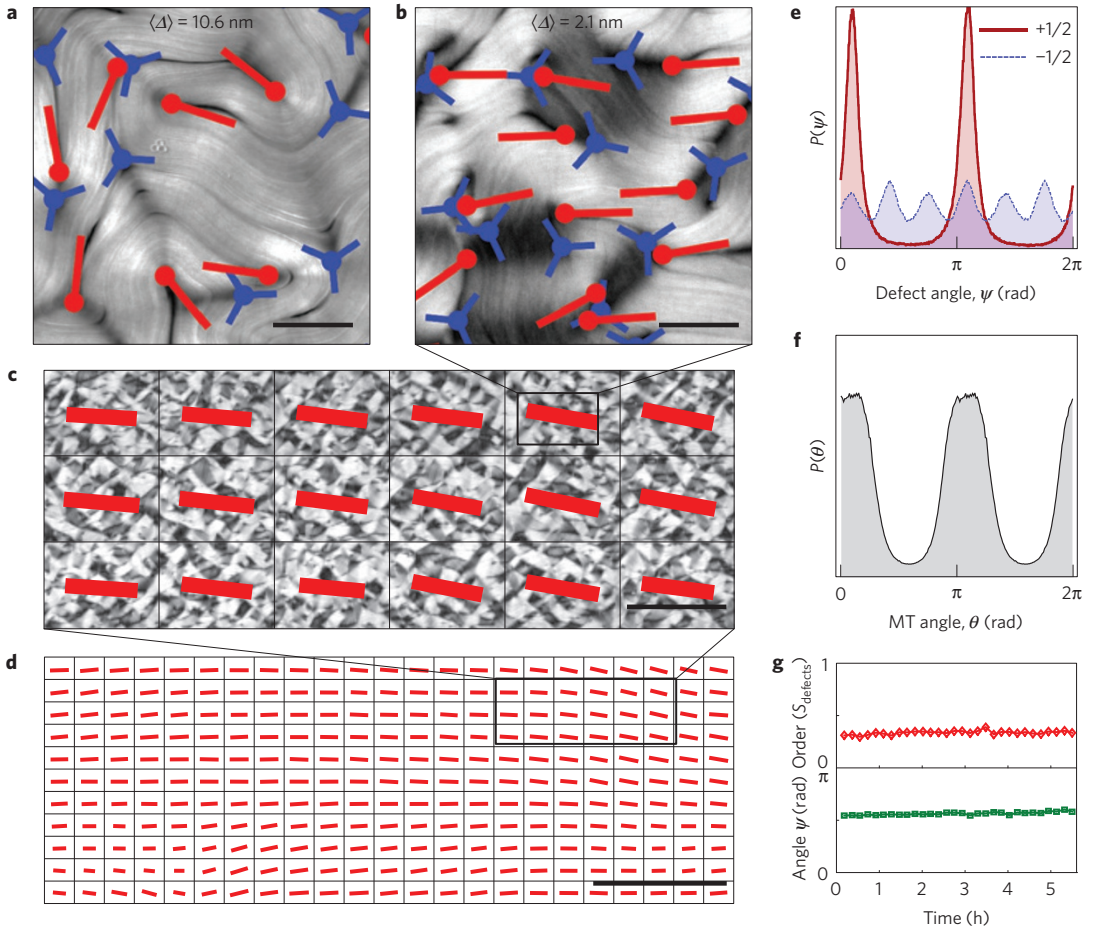

Figure 2 | Defect-ordered phase in experiments. a, Retardance map of a thick MT film in the regime of weak defect alignment. Red and blue markers indicate locations and orientations of +1/2 and −1/2 defects. Scale bar, 200 μm. **b**, Thin MT film showing strong alignment of +1/2 defects. Scale bar, 200 μm. **c**, Orientational order in a large active-nematic sample. Each red bar's orientation and length indicates the mean direction and strength of the defect alignment in one field of view. Scale bar, 2 mm. **d**, Defect alignment spans the largest samples studied (6 cm × 2 cm), containing ~20,000 defects. Scale bar, 10 mm. **e**, Normalized histogram of +1/2 (red) and −1/2 (blue) defect orientations, $P(\psi)$, for the sample shown in **b**–**d**. **f**, MT orientation, $P(\theta)$, for the sample shown in **b**–**d**. Measurements of $P(\theta)$ from 0 to π are replicated in the range from π to 2π. Both $P(\psi)$ and $P(\theta)$ show strong nematic ordering. **g**, The preferred defect orientation (green) and magnitude of the order parameter (red) averaged over a field of view persists over the entire sample lifetime.

axis (Fig. 2b). Furthermore, the orientational distribution function of −1/2 defects exhibits six-fold symmetry, although the strength of this order is significantly less than the nematic order of +1/2 defects. In addition, radial distribution functions of both ±1/2 defects reveal the absence of long-range positional order (Supplementary Fig. 9).

Next, we investigated how the orientational order of +1/2 defects persists in time and space. We find that within a single field of view (2.3 × 1.7 mm) the axis of defect order does not change appreciably over the entire sample lifetime (Fig. 2g). Therefore, we used a motorized x–y stage to repeatedly scan centimetre-sized samples every ten minutes, allowing us to measure long-range variations in defect ordering. In such samples we measure a nearly uniform system-spanning orientational order (Fig. 2c,d). The largest active-nematic sample analysed (6 cm × 2 cm) contained ~20,000 defects, demonstrating that orientational order persists at scales larger than 100 average defect spacings (Supplementary Movie 3). The defect orientational order is a result of spontaneously broken symmetry, and is not strongly influenced by the sample boundaries. To demonstrate this, we have confined active nematics in a circular geometry, finding that defects form a single uniformly aligned domain, rather than aligning with the boundaries (Supplementary Fig. 1). Consistent with these observations, we also note that active nematics in rectangular channels do not strongly favour either the long or the short axis of the channel.

In simulations, +1/2 defects also attain system-spanning orientational order (Fig. 3b,d). However, in contrast to the nematic defect ordering observed in experiments, in the computational system defects align with polar symmetry, which leads to their net transport along the preferred direction. Possible reasons for this difference are discussed below.

Tuning filament density controls the strength of the emergent defect order and can even transform the system into an isotropic state. To quantify the degree of defect ordering, we measure the 2D polar and nematic order parameters, $P = \langle \cos(\psi - \bar{\psi}) \rangle$ and $S = \langle \cos(2[\psi - \bar{\psi}]) \rangle$, respectively, where ψ is the orientation of a +1/2 defect and $\bar{\psi}$ is the mean orientation of all defects in a given system configuration. We find that thin nematic films (low MT concentration, hence low retardance) have high defect nematic order, S; increasing the film thickness (high MT concentration, high retardance) decreases the magnitude of S to the point where defects become effectively isotropic (Figs 2a,b and 4a). A similar effect is observed in simulations when varying the particle density (area fraction); at the lowest densities studied, defects have relatively strong alignment, P. Increasing density induces a transition to an isotropic state (Figs 3a,b and 4b). Spatial correlation functions of these order parameters demonstrate that, in all experimental and computational systems with measurable defect ordering, defect correlations are system-spanning (Fig. 4c,d). Although the density

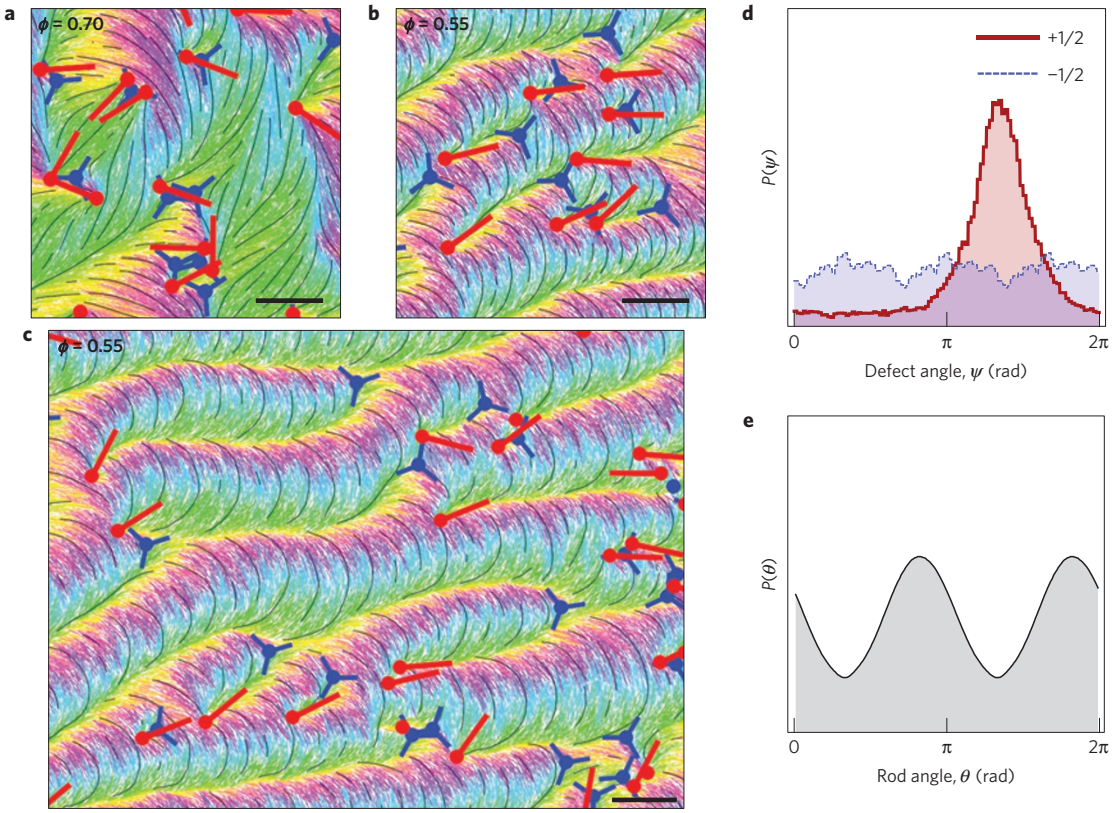

Figure 3 | Defect-ordered phase in simulations. a, Snapshot of a high-area-fraction simulation in which +1/2 defects are not aligned. Red and blue markers indicate locations and orientations of +1/2 and −1/2 defects, respectively. Scale bar, $5L_{max}$. **b**, A low-area-fraction system in which defects show flocking-like polar alignment. Scale bar, $5L_{max}$. **c**, A large simulation with defects aligned over long distances. Scale bar, $5L_{max}$. **d**, Normalized histogram of +1/2 (red) and −1/2 (blue) defect orientations, $P(\psi)$, showing polar ordering. **e**, Rod orientations $P(\theta)$ measured in the same sample, showing nematic ordering. Note that the preferred axis for the rods is offset by 90 ° from the direction of defect order. Measurements of $P(\theta)$ from 0 to π are replicated in the range from π to 2π.

of material is an easily tunable control parameter, it influences many material properties, including the rate of energy dissipation, elastic constants, and the efficiency with which active stresses are transmitted through the material, all of which influence emergent properties of the system. For example, defect density in experiments decreases weakly with the MT film thickness, whereas in simulations it increases with rod density (Supplementary Fig. 2). Further studies are required to relate the microscopic parameters to defect alignment.

In both experiment and simulation, we find that defect-ordered systems also exhibit nematic alignment of the constituent filaments (Figs 2f and 3e). The existence of such ordering in the presence of large numbers of defects contrasts sharply with equilibrium systems, in which defects reduce or eliminate nematic order. Moreover, the ordering of both defects and constituent rods decreases with system density (Fig. 4a,b and Supplementary Fig. 6), unlike in equilibrium lyotropic liquid crystals, in which order increases with density. These contrasts suggest that the orientational order in active nematics is driven by non-equilibrium dynamics, and cannot be accounted for purely by the equilibrium-like alignment of the underlying material.

Although +1/2 defects are preferentially created perpendicular to the local nematic field[32], they do not keep this orientation but are continually reoriented by their interactions with the local environment. A +1/2 defect moving through a distorted nematic field will follow a curved path, always remaining perpendicular to the field in front of it, leading to complex meandering trajectories. Simultaneously, the passage of a +1/2 defect leaves behind a distortion in which the nematic field is rotated 90° from its previous orientation, creating a topological structure which cannot relax except by the passage of further defects. These distortions strongly affect defect motion even after the defect that formed them has moved away or been annihilated. We therefore anticipate that a theory capable of explaining the origin of defect ordering will need to simultaneously account for both the defects and the underlying field.

Because our simulation model mimics the microscopic symmetries of the experiments, it is notable that the two systems exhibit different emergent symmetries. In experiments, +1/2 defects align with nematic symmetry, and the direction of defect ordering is aligned with the average MT direction (Fig. 2e,f). In simulations, defects align with polar symmetry, and the underlying rods are, on average, offset 90° from the defects (Fig. 3d,e). A number of distinctions between the two systems may account for these differences. First, analysis of the distributions of bend and splay distortions suggests that the simulation model has a much higher bend modulus (see Supplementary Information). Second, the experimental system is subjected to hard-wall boundary conditions, which preclude global polar ordering of motile defects. Third, the simulation model is dry, whereas the experiments experience hydrodynamic interactions. Finally, simulations investigate a true 2D system, whereas in experiments MTs can pass over each other. Further studies will be required to disentangle these effects.

In summary, our work demonstrates that transient, short-lived motile defects can form higher-order dynamical phases with persistent orientational order. The existence of such phases in both the experimental and computational systems suggests that this is a generic feature of active nematics.

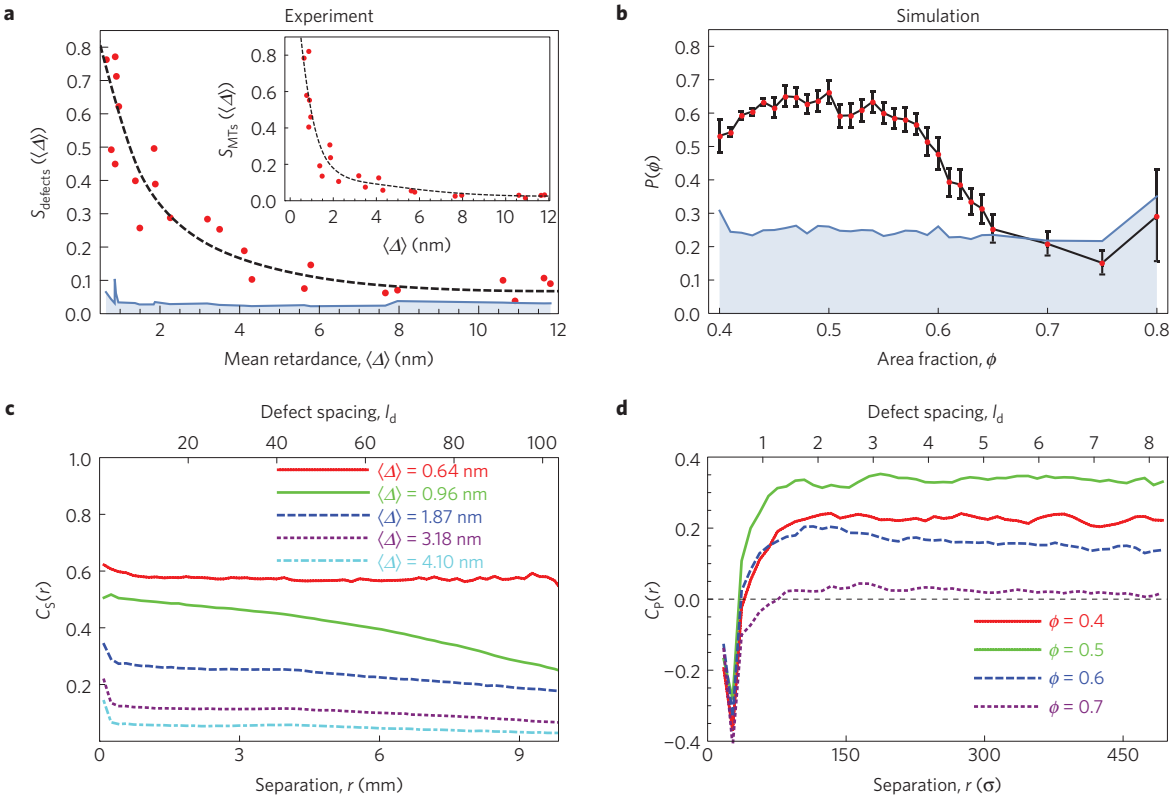

Figure 4 | Quantitative measurements of defect alignment. a, The defect nematic order parameter, *S*, decreases as a function of the MT film's mean retardance $\langle\Delta\rangle$. The blue shaded region represents the 'noise floor' (see Supplementary Information). Inset: The nematic order parameter of the underlying MT filaments, *S*, also decreases with the MT film's retardance. **b**, The polar defect order parameter, *P*, showing a transition between ordered and isotropic regimes as a function of particle density. Error bars indicate a 90% confidence interval computed by bootstrap methods, and the blue shaded region represents the 'noise floor' (see Supplementary Information for details). **c**, Two-point nematic correlation of defect orientation $C_S(r) = \langle\cos 2(\psi(\mathbf{r}) - \psi(0))\rangle$ in MT films, which shows that orientational order persists over long distances. l_d indicates the mean inter-defect spacing. The magnitude of ordering falls as retardance increases. **d**, Polar correlation of defect orientation $C_P(r) = \langle\cos(\psi(\mathbf{r}) - \psi(0))\rangle$ in simulations. σ indicates the width of a single rod (see Supplementary Information). At short ranges, defects tend to point in opposing directions, but beyond the first shell of neighbours, defects are likely to be aligned in the same direction.

Received 14 March 2015; accepted 8 July 2015; published online 17 August 2015

References

1. Narayan, V., Ramaswamy, S. & Menon, N. Long-lived giant number fluctuations in a swarming granular nematic. *Science* **317,** 105–108 (2007).
2. Duclos, G., Garcia, S., Yevick, H. G. & Silberzan, P. Perfect nematic order in confined monolayers of spindle-shaped cells. *Soft Matter* **10,** 2346–2353 (2014).
3. Zhou, S., Sokolov, A., Lavrentovich, O. D. & Aranson, I. S. Living liquid crystals. *Proc. Natl Acad. Sci. USA* **111,** 1265–1270 (2014).
4. Brugués, J. & Needleman, D. Physical basis of spindle self-organization. *Proc. Natl Acad. Sci. USA* **111,** 18496–18500 (2014).
5. Aditi Simha, R. & Ramaswamy, S. Hydrodynamic fluctuations and instabilities in ordered suspensions of self-propelled particles. *Phys. Rev. Lett.* **89,** 058101 (2002).
6. Sanchez, T., Chen, D. T. N., DeCamp, S. J., Heymann, M. & Dogic, Z. Spontaneous motion in hierarchically assembled active matter. *Nature* **491,** 431–434 (2012).
7. Giomi, L., Bowick, M. J., Ma, X. & Marchetti, M. C. Defect annihilation and proliferation in active nematics. *Phys. Rev. Lett.* **110,** 228101 (2013).
8. Thampi, S. P., Golestanian, R. & Yeomans, J. M. Velocity correlations in an active nematic. *Phys. Rev. Lett.* **111,** 118101 (2013).
9. Thampi, S. P., Golestanian, R. & Yeomans, J. M. Instabilities and topological defects in active nematics. *Europhys. Lett.* **105,** 18001 (2014).
10. Gao, T., Blackwell, R., Glaser, M. A., Betterton, M. & Shelley, M. J. Multiscale polar theory of microtubule and motor-protein assemblies. *Phys. Rev. Lett.* **114,** 048101 (2015).
11. Ngo, S. *et al.* Large-scale chaos and fluctuations in active nematics. *Phys. Rev. Lett.* **113,** 038302 (2014).
12. Chuang, I., Durrer, R., Turok, N. & Yurke, B. Cosmology in the laboratory: Defect dynamics in liquid crystals. *Science* **251,** 1336–1342 (1991).
13. Nelson, D. & Halperin, B. Dislocation-mediated melting in two dimensions. *Phys. Rev. B* **19,** 2457–2484 (1979).
14. Renn, S. R. & Lubensky, T. C. Abrikosov dislocation lattice in a model of the cholesteric to smectic-A transition. *Phys. Rev. A* **38,** 2132–2147 (1988).
15. Brandt, E. H. The flux-line lattice in superconductors. *Rep. Prog. Phys.* **58,** 1465–1594 (1995).
16. Toner, J. & Tu, Y. Long-range order in a two-dimensional dynamical XY model: How birds fly together. *Phys. Rev. Lett.* **75,** 4326–4329 (1995).
17. Toner, J., Tu, Y. & Ramaswamy, S. Hydrodynamics and phases of flocks. *Ann. Phys.* **318,** 170–244 (2005).
18. Vicsek, T. & Zafeiris, A. Collective motion. *Phys. Rep.* **517,** 71–140 (2012).
19. Marchetti, M. C. *et al.* Hydrodynamics of soft active matter. *Rev. Mod. Phys.* **85,** 1143–1189 (2013).
20. Palacci, J., Sacanna, S., Steinberg, A. P., Pine, D. J. & Chaikin, P. M. Living crystals of light-activated colloidal surfers. *Science* **339,** 936–940 (2013).
21. Redner, G. S., Hagan, M. F. & Baskaran, A. Structure and dynamics of a phase-separating active colloidal fluid. *Phys. Rev. Lett.* **110,** 055701 (2013).
22. Weber, C. a., Bock, C. & Frey, E. Defect-mediated phase transitions in active soft matter. *Phys. Rev. Lett.* **112,** 168301 (2014).
23. Wensink, H. H. *et al.* Meso-scale turbulence in living fluids. *Proc. Natl Acad. Sci. USA* **109,** 14308–14313 (2012).
24. Tjhung, E., Marenduzzo, D. & Cates, M. E. Spontaneous symmetry breaking in active droplets provides a generic route to motility. *Proc. Natl Acad. Sci. USA* **109,** 12381–12386 (2012).
25. Keber, F. C. *et al.* Topology and dynamics of active nematic vesicles. *Science* **345,** 1135–1139 (2014).

26. Nédélec, F. J., Surrey, T., Maggs, A. C. & Leibler, S. Self-organization of microtubules and motors. *Nature* **389,** 305–308 (1997).
27. Needleman, D. J. *et al.* Synchrotron X-ray diffraction study of microtubules buckling and bundling under osmotic stress: A probe of interprotofilament interactions. *Phys. Rev. Lett.* **93,** 198104 (2004).
28. Hilitski, F. *et al.* Measuring cohesion between macromolecular filaments one pair at a time: Depletion-induced microtubule bundling. *Phys. Rev. Lett.* **114,** 138102 (2015).
29. Hentrich, C. & Surrey, T. Microtubule organization by the antagonistic mitotic motors kinesin-5 and kinesin-14. *J. Cell Biol.* **189,** 465–480 (2010).
30. Shribak, M. & Oldenbourg, R. Techniques for fast and sensitive measurements of two-dimensional birefringence distributions. *Appl. Opt.* **42,** 3009–3017 (2003).
31. Bates, M. A. & Frenkel, D. Phase behavior of two-dimensional hard rod fluids. *J. Chem. Phys.* **112,** 10034 (2000).
32. Shi, X. Q. & Ma, Y. Q. Topological structure dynamics revealing collective evolution in active nematics. *Nature Commun.* **4,** 3013 (2013).

Acknowledgements

The experimental portion of this study was primarily supported by the Department of Energy, Office of Basic Energy Sciences, through award DE-SC0010432TDD (S.J.D. and Z.D.). The computational portion of this work (G.S.R., M.F.H. and A.B.) was supported by NSF-MRSEC-1420382 and NSF-DMR-1149266. Computational resources were provided by the NSF through XSEDE (Stampede and Trestles) and the Brandeis HPCC, which is partially supported by the Brandeis MRSEC (NSF-MRSEC-1420382). We acknowledge the use of a MRSEC optical and biosynthesis facility supported by NSF-MRSEC-1420382.

Author contributions

S.J.D. and Z.D. conceived the experiments and G.S.R., A.B. and M.F.H. conceived the simulations. S.J.D. acquired experimental data. G.S.R. performed computer simulations. S.J.D. and G.S.R. analysed defect dynamics. S.J.D., G.S.R., A.B., M.F.H. and Z.D. wrote the paper. All authors revised the manuscript.

Additional information

Supplementary information is available in the online version of the paper. Reprints and permissions information is available online at www.nature.com/reprints. Correspondence and requests for materials should be addressed to M.F.H. or Z.D.

Competing financial interests

The authors declare no competing financial interests.